Hyperactivated Glycolysis Drives Spatially-Patterned Kupffer Cell Depletion in MASLD

Jia He[1], Ran Li[1], Cheng Xie[1], Xiane Zhu[1], Keqin Wang[1], Zhao Shan[1]

1.Yunnan Key Laboratory of Cell Metabolism and Diseases, Center for Life Sciences, School of Life Sciences, Yunnan University, Kunming, China, 650500
*email: Zhao Shan: shanzhao@ynu.edu.cn

Declaration of interests
The authors declare no competing interests.

Financial Support
Supported by National Natural Science Foundation of China (32071129 to Z.S.), Yunnan Provincial Science and Technology Department (C619300A086 to Z.S.).

Author Contributions
JH performed the experiments, analyzed the data, and wrote the methods. RL performed inmunofluoresence staining experiments. CX, XEZ participated in sample collection. KQW helped with metabolomics analysis. ZS initiated, organized, designed the study, and wrote the manuscript.

Abstract
Metabolic dysfunction-associated steatotic liver disease (MASLD) progression is characterized by hepatic inflammation and cell death, yet the mechanisms underlying Kupffer cell (KCs) loss remain unclear. This study aims to elucidate metabolic changes behind KCs death. Using metabolomics, immunostaining, and flow cytometry, we evaluated glucose metabolic alterations and KCs death in a MASLD mouse model. Further investigation via immunostaining, Seahorse analysis, and ^{13}C-glucose isotopic tracing elucidated the glucose metabolic mechanisms underlying KCs death. Here, we demonstrate that KCs death is a hallmark feature of MASLD progression across multiple dietary models, showing significantly higher susceptibility compared to other hepatic cell types. Through comprehensive metabolic profiling, we reveal that KCs undergo progressive glucose metabolic reprogramming during MASLD development, which is correlated with KCs death. In combination of biochemical agonist, isotope tracing and KCs culture, we further demonstrated that glycolysis metabolism activation directly contributes to KCs death *in vitro*. Additionally, using genetic ablation of Chi3l1 mouse, we further demonstrated that increased glucose utilization accelerate KCs death *in vivo*. Our findings establish a correlation between glucose metabolic dynamic changes and KCs death during MASLD progression, suggesting that modulation of glucose metabolic pathways may represent a strategy to prevent KCs death and thereby alleviate MASLD.

Key words: Kupffer cells, glucose metabolism, Kupffer cell death, MASLD, glucose interaction

Introduction

Metabolic dysfunction-associated steatotic liver disease (MASLD) emerges as a prevalent liver condition in the western world, affecting roughly one-third of the population[1-3]. Its incidence continues to climb due to its strong association with obesity, type 2 diabetes, and the metabolic syndrome[4-6]. MASLD includes a spectrum of liver disorders, from metabolic dysfunction-associated

fatty liver (MAFL), often referred to as steatosis, to metabolic dysfunction-associated steatohepatitis (MASH)[7]. MASH, characterized by steatosis, inflammation, ballooning injury, and varying degrees of fibrosis, marks the initial critical stage of MASLD[8]. Kupffer cells (KCs) are liver-resident macrophages located in the hepatic sinusoids[9,10]. Derived from the embryo's yolk sac, KCs can self-renew through proliferation in adult homeostasis[11]. Studies suggest that KCs contribute to triglyceride storage during MASH progression, as demonstrated by depleting $CD207^{+}$ KCs in CD207-DTR mice using diphtheria toxin (DT) or by using $CD207^{\Delta Bcl2l1}$ mice to stimulate a low EmKCs status[12]. Upon KCs death, monocyte-derived macrophages (MoMFs) gradually seed the KCs pool and eventually replace the deceased KCs[13]. These monocyte-derived KCs (MoKCs) tend to be more inflammatory than their embryo-derived counterparts (EmKCs), altering the liver's response in MASH, eventually limiting triglyceride storage and contributing to liver cell damage[12,14]. Researchers, including our team, have observed a gradual decline in KCs during MASLD development[12,14-17]. However, little is known regarding the dynamic loss of KCs and metabolic changes behind KCs death during MASLD.

Emerging evidence highlights the fundamental role of glucose metabolism in regulating macrophages function, polarization, and survival[18-21]. Metabolic reprogramming is a well-established hallmark of macrophage activation and function in various contexts[22]. Within the unique metabolic milieu of the MASLD liver, characterized by lipotoxicity, insulin resistance, and altered nutrient fluxes, it is plausible that KCs metabolism is profoundly perturbed. Whether such metabolic shifts contribute directly to the observed KCs loss, and if so, through which specific pathways, is a crucial unanswered question.

Therefore, this study aims to investigate the hypothesis that specific metabolic changes, particularly in glucose utilization, underpin the susceptibility of KCs to death during MASLD progression. We sought to define the glucose metabolic alterations occurring in KCs as MASLD develops and to establish a direct causal link between these metabolic reprogramming events and KCs demise. Elucidating these mechanisms is essential for understanding MASLD pathogenesis and identifying novel therapeutic targets aimed at preserving hepatic immune homeostasis.

Materials and methods

Animal experiments and procedures

Animals *Chil1*$^{-/-}$ (strain no. T014402), *Chil1*$^{flox//flox}$ (strain no. T013652), and *Clec4f-cre* (strain no. T036801) mice with a *C57BL/6J* background were purchased from GemPharmatech. Accordingly, *C57BL/6J* mice (strain no. N000013) were used as wild-type (WT) mice. To generate *Clec4f*$^{\Delta Chil1}$ mice, *Chil1*$^{flox//flox}$ mice were crossed with *Clec4f-cre* mice and knock out efficiency was examined in KCs previously[17]. All mouse colonies were maintained at the Animal Core Facility of Yunnan University. The animal studies were approved by the Yunnan University Institutional Animal Care and Use Committee (IACUC, Approval No. YNU20220314). Male mice aged 6-8 weeks were used in this study.

Construction of MASLD/MASH mouse model Mice were provided a high-fat and high-cholesterol diet (Research Diet, d12108c, 40 kcal% fat and 1.25% cholesterol) or a high-fat diet (Research Diet,

d12492, 60 kcal% fat). Another group of mice was fed a methionine and choline deficient diet (Research Diet, A02082002BR) for 6 weeks. Throughout the feeding period, the body weight and food consumption of the mice were observed and recorded weekly. Once the dietary intervention was completed, the mice were euthanized. Liver and murine serum samples were collected for further analysis. Alanine aminotransferase (ALT) and aspartate aminotransferase (AST) levels in the serum, as well as cholesterol (TC) and triglyceride (TG) levels in both serum and liver tissues, were quantified using commercially available kits (Nanjing Jiancheng Bioengineering Institute). Genotyping Sample preparation and procedure were conducted as previously described[17].

Kupffer Cell Processing and Metabolomic Profiling

Primary KCs were isolated from livers of HFHC-fed mice at 0, 4, and 8 weeks using established protocols. After a 15-min adherence period, cells were washed twice with ice-cold PBS and detached using 1 mL ice-cold PBS followed by gentle scraping. Cell suspensions were transferred to 1.5 mL tubes, and 3×10^6 cells were pelleted by centrifugation (1,000 × g, 5 min). Supernatants were discarded, and pellets snap-frozen in liquid nitrogen. Metabolites were extracted from frozen pellets with 80% methanol (vol/vol) and analyzed via LC–MS/MS using an AB Sciex 6500 Plus QTRAP mass spectrometer coupled to an ExionLC system. All metabolomic processing and data analysis were performed by BioDeep (https://www.biodeep.cn).

Isotope Tracing

For ^{13}C-tracing experiments, BMDMs were isolated from WT and *Chil1*$^{-/-}$ mice, cultured to maturity, and replated. After 12 hours, cells were incubated for 12 hours in glucose-depleted medium supplemented with 10% dialyzed FBS and 15 mmol/L universally labeled [U-^{13}C]glucose (Cambridge Isotope Laboratories, CLM-1396-1). Cells were subsequently washed twice with ice-cold glucose-free medium. Following supernatant removal, metabolites were extracted using pre-cooled 80% (vol/vol) methanol for cell lysis.

Metabolite separation was performed using a Vanquish UHPLC system (Thermo Fisher Scientific) equipped with an Amide column (Waters). The mobile phase consisted of: (A) 10 mM ammonium acetate and 0.3% ammonia in water, and (B) 10 mM ammonium acetate and 0.3% ammonia in 90% acetonitrile. Metabolites were separated using a linear gradient elution. Metabolites were ionized, and mass spectrometry data were acquired using an Orbitrap Fusion Tribrid mass spectrometer (Thermo Fisher Scientific). Targeted metabolite analysis was performed by LC–MS/MS using a QTRAP 5500+ system (SCIEX) coupled to an ExionLC AD UHPLC system (SCIEX). Isotope tracing analysis and metabolomic data processing were conducted by BioDeep using the BioDeep Platform (https://www.biodeep.cn).

Spatial Analysis of KCs Death

To evaluate the spatial distribution of KCs death along the portal-central axis, the distance between the portal vein (PV) and central vein (CV) was measured in histological sections. The PV-CV axis was systematically divided into three equidistant zones (periportal, intermediate, and pericentral) for regional analysis. KCs death was quantified by isolating fluorescence signals corresponding to cell death markers (Tunel) through channel thresholding and noise reduction. The positive area and integrated fluorescence intensity were measured within each zone, excluding vascular structures to

focus on parenchymal KCs populations. This zonal approach enabled comparative assessment of KCs death patterns across different hepatic microenvironments.

Diagnosis of MASLD activity score

Murine MASLD activity was assessed histologically using the NAFLD Activity Score (NAS) on hematoxylin and eosin (H&E) stained liver sections following features: hepatocyte ballooning degeneration (0-2), lobular inflammation (0-3), and steatosis grade (0-3)[23]. The individual scores were summed to yield the total NAS (range 0-8) per animal. A NAS ≥ 5 was considered diagnostic for steatohepatitis (MASH), NAS ≤ 3 indicated not-MASH, and NAS = 4 was indeterminate.

Data Presentation and Statistical Analysis

Data in graph figures are presented as mean ± standard error of the mean (SEM). Statistical analyses were performed using SPSS Statistics (Version 22). For comparisons between two groups, an unpaired two-tailed Student's t-test was used, while one-way analysis of variance (ANOVA) was applied for comparisons involving three or more groups. A p-value < 0.05 was considered statistically significant, with p-values indicated where applicable. All cell culture experiments were repeated at least three times independently. Figure 7 was created using the Figdraw platform (www.figdraw.com).

Additional Methods

Additional detailed methods can be found in the Supporting Information.

Results

The death of Kupffer cells is a pathological characteristic during MASLD.

To systematically investigate KCs death, we established an MASLD mouse model by feeding C57Bl/6J mice a high-fat high-cholesterol diet (HFHC) (Figure S1A). After 4 or 16 weeks of HFHC feeding, we conducted Hematoxylin/eosin (H&E), Oil Red o and Sirius red staining to assess immune cell infiltration, fat accumulation, and liver fibrosis. At 4 weeks of HFHC feeding, we observed a slight increase in lipid droplets, with no apparent signs of liver inflammation or fibrosis in hepatocytes (Figure S1A). However, by 16 weeks of HFHC feeding, both lipid droplets and immune cell infiltration had significantly increased, though liver fibrosis was still absent and MASLD activity score is below 4 (Figure S1A). Moreover, the body weight of mice fed HFHC gradually increased over the feeding period (Figure S1B). Analysis of serum alanine aminotransferase (ALT), aspartate aminotransferase (AST), serum and liver cholesterol or liver triglyceride (TG) levels revealed significant increases compared to mice fed a normal chow diet (NCD), except for serum TG, which is similar between NCD and HFHC-fed mice (Figure S1D). These findings collectively indicate the successful establishment of an early MASLD mouse model, without fibrosis development yet.

Subsequently, we investigated KCs death by labeling KCs with antibodies targeting C-type lectin domain family 4 (Clec4f), a protein specific to KCs[13], and employing TdT-mediated dUTP Nick-End Labeling (Tunel), a method for detecting dead cells. Compared to baseline (0 weeks, prior to HFHC diet), KCs death was evident as early as 4 weeks, with nearly 60% of KCs undergoing cell death by 16 weeks post HFHC feeding (Figure 1A, 1B). To further validate KCs death during

MASLD progression, we performed co-staining of the apoptotic marker cleaved caspase-3 (Cl-Casp3) with Clec4f. This analysis confirmed a significant increase in apoptotic KCs during HFHC diet feeding (Figure S2A).Considering the potential recruitment of monocyte-derived macrophages (MoMFs) into the liver, which may acquire KC features, including Clec4f expression[12,14], we included another marker specifically expressed by KCs, T cell immunoglobulin mucin protein 4 (Timd-4)[12,24]. Flow cytometry analysis of liver nonparenchymal cells (NPCs) was performed to discriminate between KCs and MoMFs. KCs were identified as $CD45^+$ $F4/80^{hi}$ $CD11b^{low}$ $Timd4^+$ cells, while MoMFs were identified as $CD45^+$ $F4/80^+$ $CD11b^{hi}$ $Timd4^-$ cells (Figure 1C). Consistent with the staining results, the number of KCs decreased as early as 4 weeks and continued to decline until 16 weeks on the HFHC diet (Figure 1C, 1D). The infiltration of MoMFs into the liver occurred gradually and followed the onset of KCs death (Figure S2B, S2C). To assess proliferation-associated Tunel false positivity, we evaluated Ki67 expression in dying KCs ($Tunel^+Timd4^+$). Two critical observations emerged: Proliferating KCs ($Ki67^+Timd4^+$) were rare under baseline and HFHC conditions. Only a minor fraction (<20%) of $Tunel^+Timd4^+$ KCs co-expressed Ki67, indicating that the majority of $Tunel^+$ KCs represent true cell death events rather than proliferation-related artifacts (Figure S2D).

Furthermore, we examined KCs death in several other MASLD mouse models, including mice fed a high-fat diet (HFD) for 16 weeks[25] and a methionine/choline deficient diet (MCD) for 6 weeks[12]. Co-staining of Clec4f and Tunel in liver sections revealed a notable increase in KCs death in both the HFD and MCD groups compared to the control group fed a normal chow diet (NCD) (Figure 1E, 1F). These findings collectively confirm that progressive KCs death is a pathological hallmark of MASLD observed in various dietary-induced models.

Kupffer cells exhibit spatially-patterned vulnerability in MASLD

To assess relative susceptibility of hepatic cell populations, diet-induced cell death was quantified via Tunel co-staining with lineage markers: HNF4α (hepatocytes), Desmin (hepatic stellate cells; HSCs), and Iba1 (monocyte-derived macrophages; MoMFs) (Figure 2A–C). Hepatocyte death showed minimal change during the initial 4 weeks but increased modestly by 16 weeks (Figure 2A). In contrast, HSCs and MoMFs mortality rose progressively throughout MASLD progression, with significant increases detectable as early as 4 weeks (Figure 2B, 2C). Notably, KCs exhibited the highest cell death incidence among all evaluated populations, highlighting their exceptional vulnerability.

We next determined whether KCs mortality displays spatial zonation. Leveraging the liver's lobular architecture—organized into periportal (PP, zone 1), midzonal (Mid, zone 2), and pericentral (PC, zone 3) hepatocyte zones[26]—we performed co-staining for Timd4 (KCs marker), Tunel, and glutamine synthetase (GS; central vein marker) (Figure 2D). KCs death increased temporally across all zones, consistent with prior Clec4f/Tunel data. Strikingly, spatial analysis revealed significant periportal predominance, with PP mortality rates exceeding GS^+ PC zones at 16 weeks of HFHC feeding (Figure 2D). These findings establish KCs as the most vulnerable hepatic population in MASLD and uncover a spatially-distinct periportal mortality pattern.

Kupffer cells exhibit metabolic reprogramming with increased glycolysis during early

MASLD.

To elucidate glucose metabolism changes behind KCs death during MASLD, we isolated KCs from mice at various time points during HFHC feeding (0, 4, 8, and 16 weeks). The purity of isolated KCs was confirmed by Timd4 immunofluorescence staining, with Timd4+ cells reaching over 90% (Figure S3A). Subsequently, we conducted a qRT-PCR assay to assess the mRNA expression levels of key enzymes involved in glycolysis (*Slc2a1, Hk3, Pfkfb3, Pkm*), the pentose phosphate pathway (PPP) (*G6pd, 6pdg*), glycogenolysis (*Pygl*), and glycogenesis (*Gys1, Ugp2*). Our data revealed that the mRNA expression of rate-limiting enzymes associated with fast glucose metabolism, such as glycolysis and PPP, significantly increased as early as 8 weeks after HFHC feeding initiation (Figure S3B). While mRNA expression of glycolysis rate-limiting enzymes remained elevated, PPP expression began to decline by 16 weeks after HFHC feeding (Figure S3B). Conversely, enzymes linked to slow glucose metabolism, such as oxidative phosphorylation (*Idh1, Ogdh*), did not exhibit significant changes (Figure S3B). Furthermore, mRNA expression of glycogenesis and glycogenolysis rate-limiting enzymes started to decrease at 8 and 16 weeks after HFHC feeding, respectively, suggesting that glucose uptake becomes the primary source of glucose metabolism in KCs during this period (Figure S3B). In addition, we investigated the mRNA expression of rate-limiting enzymes involved in β-oxidation (*Acadm, Hadh*) but found no significant differences (Figure S3B). The data suggest a time-dependent metabolic inflexibility, where impaired glycogen handling and mitochondrial inertia drive sustained glycolytic dependence in KCs, which exacerbate KCs vulnerability (especially in periportal zones, where glycogen storage is predominant[27]).

To validate KCs-specific metabolic alterations in MASLD, we performed metabolomic analysis on primary KCs from male wild-type mice fed an HFHC diet for 0, 4, or 8 weeks (Figure 3A). Given that KCs mortality peaked at 8 weeks in our model (Figure 2D), we focused on these early time points to capture initiating metabolic shifts. Principal component analysis (PCA) of KCs metabolites revealed distinct, diet duration-dependent clustering, indicating profound remodeling of the global metabolic landscape (Figure 3B). Kyoto Encyclopedia of Genes and Genomes (KEGG) pathway enrichment analysis identified glucose metabolism pathways—including glycolysis and the pentose phosphate pathway (PPP)—as the most significantly upregulated during MASLD progression (Figure 3C, 3D). This glycolytic activation was further corroborated by time-dependent accumulation of key intermediates (glucose, Phosphatidylethylamine [PEA], Phosphoenolpyruvate [PEP], fructose-1,6-bisphosphate [FBP], and lactate [LA]) in heatmap analysis (Figure 3E). Critically, we observed progressive increases in death-executing metabolites generated through these glucose metabolism pathways: redox disruptors (GSSG, FAD), mitochondrial toxins (methylmalonic acid), and apoptosis mediators (Hcy) - all exhibiting temporal coupling with glycolytic intermediates (Figure 3F). This demonstrates that KCs undergo rapid glycolytic reprogramming during early MASLD pathogenesis that actively generates cytotoxic effectors, coinciding with their peak vulnerability.

Excessive glucose metabolic activity contributes to Kupffer cell death.

To investigate the direct role of glucose activation in KCs death, isolated Kupffer cells were subjected to *in vitro* metabolic perturbations. First, KCs were treated with combinations of glucose and palmic acid (PA) to model MASLD pathology. Physiological glucose (5.5 mM) combined with PA increased KCs death by approximately 10%. Strikingly, elevating glucose to serum levels

observed during HFHC feeding (10 mM) further increased KCs death by approximately 27%. This was evidenced by increased Cleaved Caspase-3 (Cl-Casp3) staining (Figure 4A) and elevated Cl-Casp3 protein levels via Western blot (Figure 4B).

Second, we treated KCs with the PDK1 activator PS48, which directly stimulates glycolysis. The results indicated a markedly increased KCs death compared to blank or DMSO vehicle controls (Figure 4C, 4D). Finally, Oligomycin (ATP synthase inhibitor) was used to force glycolytic reliance by blocking mitochondrial ATP production. Oligomycin treatment similarly induced significant KCs death (Figure 4E and F), phenocopying the effects of direct glycolytic activation. Collectively, these data demonstrate that both excessive glycolytic flux (induced by high glucose or PDK1 activation) and impaired mitochondrial ATP production (inducing compensatory glycolysis) promote KCs death.

Enhanced glycolytic flux in *Chil1*$^{-/-}$ macrophages.

To investigate whether hyperactivated glycolysis drives KCs death *in vivo*, we focused on Chitinase 3-like 1 (Chi3l1; gene *Chil1*)—a glucose uptake regulator conserved across macrophage populations, including KCs and BMDMs[17]. Given the limited availability of primary KCs for intensive isotopic tracing ([U-^{13}C]glucose assays) and the shared susceptibility of MoMFs to MASLD-induced death (Figure 2C), we employed *Chil1*$^{-/-}$ BMDMs as a validated model to dissect Chi3l1-dependent metabolic mechanisms. Uniformly labeled [U-^{13}C]glucose tracer analysis (Figure 5A) in *Chil1*$^{-/-}$ BMDMs revealed genotype-specific metabolic reprogramming: PCA showed distinct clustering versus wild-type (WT) (Figure 5B), while heatmaps demonstrated pronounced accumulation of glycolytic intermediates (Figure 5C). Metabolic flux quantification confirmed significantly elevated U-^{13}C enrichment in glycolytic metabolites—including glucose (Glc), fructose-6-phosphate (F6P), 3-phosphoglycerate (3PGA), 2-phosphoglycerate (2PGA), phosphoenolpyruvate (PEP), pyruvate (PA), and lactate (LA)—whereas glucose-6-phosphate (G6P), fructose-1,6-bisphosphate (FBP), and pentose phosphate pathway (PPP) intermediates (ribulose-5-phosphate [Ru5P], ribose-5-phosphate [R5P], sedoheptulose-7-phosphate [S7P]) remained unchanged. Dihydroxyacetone phosphate (DHAP) was the sole PPP-linked metabolite showing increased enrichment (Figure 5D), indicating *Chil1* deletion selectively hyperactivates glycolysis without engaging the PPP. Moreover, extracellular acidification rates (ECAR) analysis also showed significantly elevated glycolytic capacity in *Chil1*$^{-/-}$ BMDMs (Figure 5 E, 5F).

Given our prior demonstration that Chi3l1 functions mainly as a secretory regulator of macrophages glucose metabolism[17]. Therefore, we also added recombinant Chi3l1(rChi3l1) supplementation group. rChi3l1 supplementation reversed hyper-glycolytic flux, restoring levels comparable to WT (Figure S4A-S4D). Glycolytic intermediates (Glc, F6P, FBP, 3PGA, 2PGA, PEP, PA, LA, G6P) showed reduced mass isotopologue distributions (Figure S4B, S4C). PPP intermediates (Ru5P, R5P, S7P, DHAP) remained unaffected (Figure S4B, S4C), reinforcing pathway specificity. Functionally, rChi3l1 significantly reduced lactate dehydrogenase (LDH) activity in high glucose-treated BMDMs, confirming attenuated glycolytic output (Figure S4D). Collectively, these data establish that Chi3l1 deletion specifically enhances glycolytic flux—but not PPP activity—in macrophages, positioning it as a mechanistic model for investigating glycolysis-driven KCs death.

Enhanced glycolysis accelerated Kupffer cell death in MASLD.

Next, we employed *Chil1*$^{-/-}$ mice as a mechanistic model to investigate glycolysis-driven KCs death. First, we isolated primary KCs from WT and *Chil1*$^{-/-}$ mice and treated them with PA. *Chil1*$^{-/-}$KCs exhibited significantly increased susceptibility to PA-induced cell death compared to WT controls *in vitro* (Figure 6A). This heightened vulnerability was quantified through elevated Cl-Casp3 immunostaining (Figure 6B) and increased LDH release (Figure 6C), confirming enhanced cell death. We previously reported that KCs death increased in *Chil1*$^{-/-}$ (Chil1 is deficient in whole body) mouse during MASLD[17]. To definitively determine the cellular source of Chi3l1 in MASLD livers, we performed systematic immunohistochemical analysis of serially sectioned tissues from mice fed an HFHC diet for 16 weeks. Consecutive sections were independently probed for Chi3l1 or lineage-specific markers (HNF4α, Desmin, Iba1), enabling cellular localization through morphological alignment across sequential slices. The results revealed predominant Chi3l1 expression in hepatic macrophages, especially KCs (Figure S5A). Moreover, Chi3l1 expression was significantly elevated in KCs during MASLD progression, as evidenced by co-staining with F4/80 and Timd4 (Figure S5B). These findings suggest Chi3l1 might be a KCs-autonomous regulator protein. To determine cell-autonomous effects, we generated KCs-specific Chil1 knockout mice (*Clec4f*$^{\Delta Chil1}$ mice) and analyzed their response to HFHC feeding. Flow cytometry of non-parenchymal cells (NPCs) revealed significant lower of the KCs compartment (CD45^{+} F4/80^{hi} CD11b^{low} Timd4^{+}) in *Clec4f*$^{\Delta Chil1}$ mice after 16 weeks of HFHC diet compared to Clec4f^{cre} controls (Figure 6D). This KCs loss was corroborated by Timd4/Tunel co-staining, which showed elevated KCs death in *Clec4f*$^{\Delta Chil1}$ livers (Figure 6F, 6G). Collectively, these findings demonstrate that genetic ablation of Chil1 amplifies glycolytic flux, sensitizes KCs to lipotoxic stress *in vitro*, and drives KCs depletion through accelerated cell death *in vivo*, establishing Chi3l1 as a critical cell-autonomous regulator of KCs survival in MASLD.

Discussion

This study establishes that KCs death is an early pathological feature of MASLD across multiple dietary models, exhibiting significantly greater susceptibility in KCs compared to other hepatic cell types. Through integrated transcriptomic, metabolomic, and functional analyses, we reveal that KCs undergo profound metabolic reprogramming characterized by progressive activation of glycolytic metabolism during MASLD development. Crucially, we provide compelling *in vitro* evidence that direct glycolytic activation (via high glucose, the PDK1 agonist PS48) or enforced glycolytic dependence (via mitochondrial ATP synthase inhibition with oligomycin) significantly exacerbates KCs apoptosis. Complementing this, *in vivo* studies utilizing genetic ablation of Chi3l1 – a KCs glucose-uptake inhibitor– amplifies glycolytic metabolism and accelerates diet-induced KCs loss. Collectively, these findings delineate hyperactivation of glycolysis as a central mechanism underpinning the unique vulnerability and depletion of KCs in MASLD (Figure 7).

Our observation of preferential periportal KCs death aligns with the portal vein's role as the primary entry point for dietary nutrients, including glucose and lipids[26,28]. This spatial pattern suggests that KCs in this zone face the earliest and highest concentrations of metabolic stressors from the HFHC diet, potentially overwhelming their regulatory capacity. The heightened susceptibility of KCs relative to other hepatic cell types likely stems from their specialized functions as resident macrophages, including constant immune surveillance and phagocytosis, which may impose distinct

metabolic demands and sensitivities[29,30]. While metabolic reprogramming towards glycolysis is a recognized feature of activated macrophages (often linked to pro-inflammatory phenotypes)[15], our findings reveal a critical divergence: in KCs during MASLD, sustained glycolytic hyperactivation culminates not in sustained activation, but in apoptotic cell death. This highlights a unique metabolic vulnerability specific to KCs in the context of chronic nutrient overload.

Previous studies demonstrate Chi3l1's pro-fibrotic role in advanced MASH, where it stimulates hepatic stellate cells via IL-13Rα2 (CDAA-HFAT model
)[31], inhibits macrophage apoptosis through Fas/Akt signaling (CCL4 and MCD models)[32], and directly promotes fibrogenesis in aging livers[33]. In contrast, our work reveals Chi3l1's protective metabolic function in early MASLD using an HFHC model that recapitulates steatohepatitis without fibrosis (Fig S1A). While myeloid-specific deletion (*Lysm*$^{\Delta Chil1}$ mice) showed no metabolic phenotype[17], KCs-specific ablation (*Clec4f*$^{\Delta Chil1}$) accelerated KCs loss and steatosis progression. This establishes Chi3l1 as a KCs-autonomous guardian that restrains glycolytic overload—a mechanism distinct from its anti-apoptotic effects in fibrotic contexts. This apparent duality arises from disease-stage specificity: In pre-fibrotic MASLD, KCs-derived Chi3l1 sustains metabolic homeostasis by preventing lethal hyper-glycolysis. In established fibrosis, MoMFs-derived Chi3l1 drives ECM remodeling. Our data thus reconcile prior contradictions: Chi3l1's role transitions from hepatoprotective in early disease (via KCs survival) to pro-fibrotic in advanced MASH (via MoMFs-HSCs crosstalk), with outcomes determined by cellular source and pathological context.

Our recent study demonstrated that KCs exhibit a glucose-hungry metabolic phenotype, making them uniquely dependent on Chi3l1-mediated regulation. In contrast, MoMFs maintain a relatively glucose-independent metabolic program[17]. Complementing these findings, current data confirm that Chi3l1 loss resulted in increased glycolytic flux (measured by ^{13}C-glucose tracing) in KCs and markedly increased sensitivity to lipotoxicity *in vitro* and accelerated death in *vivo*. This establishes Chi3l1 as a critical cell-autonomous regulator of KCs glucose metabolism, restraining glycolysis and promoting survival under metabolic stress. Identifying Chi3l1 as a guardian of KCs glucose homeostasis provides crucial insight into their metabolic resilience. While Chi3l1 regulates glucose uptake across macrophage subtypes (including BMDMs), its loss is selectively detrimental to KCs due to their unique reliance on glucose metabolism. This dichotomy arises from intrinsic differences in metabolic programming, not divergent Chi3l1 functions.

While Chi3l1 regulates glucose uptake across macrophage subtypes (including BMDMs), its loss disproportionately compromises KCs survival due to their intrinsic metabolic inflexibility—not divergent Chi3l1 functions. This mechanistic distinction explains why MoMFs (and BMDMs) tolerate Chi3l1 deficiency: their metabolic plasticity allows adaptation to glucose fluctuations, whereas KCs undergo energetic crisis when glycolytic control fails[17]. Crucially, our experimental data demonstrate that: Chi3l1 loss hyperactivates glycolytic flux in BMDMs (confirmed by U^{13}C-glucose tracing), establishing a conserved regulatory mechanism relevant to KCs. This metabolic dysregulation directly increases KCs sensitivity to lipotoxicity *in vitro* and accelerates death *in vivo*. KCs-specific Chi3l1 ablation (*Clec4f*$^{\Delta Chil1}$) triggered progressive KCs depletion under metabolic stress. Collectively, these findings establish Chi3l1 as a cell-autonomous guardian of KCs glucose homeostasis.

Several limitations of this study should be acknowledged. Firstly, while we utilized multiple dietary models (HFHC, HFD, MCD), the findings are derived from mouse studies. Validation in human MASLD/NASH samples, particularly assessing spatial KCs death patterns and Chi3l1 expression/metabolic signatures in human KCs, is essential. Secondly, while we establish glycolysis as a key driver, the precise downstream mechanisms linking hyper-glycolysis to apoptosis in KCs remain to be fully elucidated. Potential mediators include excessive reactive oxygen species (ROS) generation, lactate accumulation and acidosis, alterations in NAD+/NADH ratios, or insufficient ATP production despite high flux if mitochondrial capacity is compromised. Thirdly, our study focused primarily on glucose metabolism; the potential contribution of altered fatty acid oxidation or amino acid metabolism to KCs death warrants further exploration.

Despite these limitations, our findings have significant translational implications. They suggest that interventions aimed at modulating KCs glucose metabolism, rather than merely suppressing inflammation, could be a novel therapeutic strategy for MASLD. Potential approaches include enhancing Chi3l1 signaling or activity, selectively inhibiting key glycolytic drivers (e.g., PDK1) within KCs, or providing metabolic support to bolster KCs survival under stress. Preserving the KCs population could help maintain immune homeostasis, dampen chronic inflammation, and potentially slow or prevent MASLD progression. Future research should focus on: 1) Validating the human relevance of KCs metabolic vulnerability and Chi3l1's role; 2) Defining the exact glycolytic checkpoints and downstream effectors triggering KCs apoptosis; 3) Developing and testing targeted strategies to modulate KCs glycolysis *in vivo*; and 4) Investigating the long-term functional impact of preventing KCs death on overall MASLD histopathology and progression.

In conclusion, this study uncovers a fundamental mechanism of MASLD pathogenesis: metabolic reprogramming towards hyper-glycolysis renders Kupffer cells uniquely susceptible to apoptosis, leading to their progressive depletion, particularly in the periportal region. Chi3l1 serves as a critical endogenous regulator restraining this lethal metabolic shift. Targeting this KCs-specific metabolic vulnerability represents a promising avenue for developing novel therapies aimed at preserving hepatic immune function and halting MASLD progression.

Abbreviations

MASLD, metabolic dysfunction-associated fatty liver disease; MASH, metabolic dysfunction-associated steatohepatitis; KCs, Kupffer cells; Chi3l1, Chitinase 3 like 1; ALT, Alanine aminotransferase; AST, aspartate aminotransferase; TC, cholesterol; TG, triglyceride; NPCs, nonparenchymal cells; HFHC, high fat high cholesterol diet; NCD, normal chow diet; Clec4f, C-type lectin domain family 4; Timd-4,T cell immunoglobulin mucin protein 4; MoMFs, monocyte-derived macrophages; HFD, high-fat diet; MCD, methionine/choline deficient diet; WD, western diet; PPP, pentose phosphate pathway; BMDM, bone marrow derived macrophages; DMSO, dimethyl sulfoxide; MAFL, non-alcoholic fatty liver; rChi3l1, recombinant murine Chi3l1; PA, palmic acid; Iso, Isopropyl alcohol; MoKCs, monocytes-derived Kupffer cells; ALD, alcohol-induced liver disease; AILI, acetaminophen-induced liver injury; EmKCs, embryo-derived Kupffer cells; DT, diphtheria toxin; WT, wild-type; TUNEL, TdT-mediated dUTP Nick-End Labeling;

Acknowledgements

We thank Dr. Bin Qi (Yunnan University) for suggestions and discussion. We thank Guangxun Meng (The Shanghai Institute of Immunity and Infection of the Chinese Academy of Sciences) for providing us with L929 cells. We thank Cynthia Ju (UTHealth) for advice in manuscript submission.

Reference

1 Hardy, T., Oakley, F., Anstee, Q. M. & Day, C. P. Nonalcoholic Fatty Liver Disease: Pathogenesis and Disease Spectrum. *Annu Rev Pathol-Mech* **11**, 451-496, doi:10.1146/annurev-pathol-012615-044224 (2016).

2 Younossi, Z. *et al.* Global burden of NAFLD and NASH: trends, predictions, risk factors and prevention. *Nat Rev Gastro Hepat* **15**, 11-20, doi:10.1038/nrgastro.2017.109 (2018).

3 Younossi, Z. M. Non-alcoholic fatty liver disease - A global public health perspective. *J Hepatol* **70**, 531-544, doi:10.1016/j.jhep.2018.10.033 (2019).

4 Rinella, M. E. & Sanyal, A. J. Management of NAFLD: a stage-based approach. *Nat Rev Gastro Hepat* **13**, 196-205, doi:10.1038/nrgastro.2016.3 (2016).

5 Sheka, A. C. *et al.* Nonalcoholic Steatohepatitis: A Review. *Jama-J Am Med Assoc* **323**, 1175-1183, doi:10.1001/jama.2020.2298 (2020).

6 Eslam, M. *et al.* A new definition for metabolic dysfunction-associated fatty liver disease: An international expert consensus statement. *Journal of Hepatology* **73**, 202-209, doi:10.1016/j.jhep.2020.03.039 (2020).

7 Eslam, M., Sanyal, A. J., George, J. & Panel, I. C. MAFLD: A Consensus-Driven Proposed Nomenclature for Metabolic Associated Fatty Liver Disease. *Gastroenterology* **158**, 1999-+ (2020).

8 Friedman, S. L., Neuschwander-Tetri, B. A., Rinella, M. & Sanyal, A. J. Mechanisms of NAFLD development and therapeutic strategies. *Nature Medicine* **24**, 908-922, doi:10.1038/s41591-018-0104-9 (2018).

9 Kazankov, K. *et al.* The role of macrophages in nonalcoholic fatty liver disease and nonalcoholic steatohepatitis. *Nature reviews. Gastroenterology & hepatology* **16**, 145-159, doi:10.1038/s41575-018-0082-x (2019).

10 Gomez Perdiguero, E. *et al.* Tissue-resident macrophages originate from yolk-sac-derived erythro-myeloid progenitors. *Nature* **518**, 547-551, doi:10.1038/nature13989 (2015).

11 Hashimoto, D. *et al.* Tissue-Resident Macrophages Self-Maintain Locally throughout Adult Life with Minimal Contribution from Circulating Monocytes. *Immunity* **38**, 792-804, doi:10.1016/j.immuni.2013.04.004 (2013).

12 Tran, S. *et al.* Impaired Kupffer Cell Self-Renewal Alters the Liver Response to Lipid Overload during Non-alcoholic Steatohepatitis. *Immunity* **53**, 627-640.e625, doi:10.1016/j.immuni.2020.06.003 (2020).

13 Scott, C. L. *et al.* Bone marrow-derived monocytes give rise to self-renewing and fully differentiated Kupffer cells. *Nat Commun* **7**, 10321, doi:10.1038/ncomms10321 (2016).

14 Daemen, S. *et al.* Dynamic Shifts in the Composition of Resident and Recruited Macrophages Influence Tissue Remodeling in NASH. *Cell reports* **34**, 108626, doi:10.1016/j.celrep.2020.108626 (2021).

15 Tacke, F. Targeting hepatic macrophages to treat liver diseases. *Journal of hepatology* **66**, 1300-1312, doi:10.1016/j.jhep.2017.02.026 (2017).

16 Remmerie, A. *et al.* Osteopontin Expression Identifies a Subset of Recruited Macrophages

Distinct from Kupffer Cells in the Fatty Liver. *Immunity* **53**, 641-657.e614, doi:10.1016/j.immuni.2020.08.004 (2020).

17 Jia He, B. C., Xiong Wang, Ruoxue Yang, Chengxiang Deng, Xiane Zhu, Keqin Wang, Lang Wang, Xiaokang Lu, Cheng Peng, Canpeng Li, Zhao Shan. Differential Regulation of Hepatic Macrophage Fate by Chi3l1 in MASLD. *eLife* **14**, doi:https://doi.org/10.7554/eLife.107023.1 (2025).

18 Faas, M. *et al.* IL-33-induced metabolic reprogramming controls the differentiation of alternatively activated macrophages and the resolution of inflammation. *Immunity* **54**, 2531, doi:10.1016/j.immuni.2021.09.010 (2021).

19 Du, L. *et al.* IGF-2 preprograms maturing macrophages to acquire oxidative phosphorylation-dependent anti-inflammatory properties. *European Journal of Immunology* **49**, 491-491 (2019).

20 Woods, P. S. *et al.* HIF-1α induces glycolytic reprograming in tissue-resident alveolar macrophages to promote cell survival during acute lung injury. *Elife* **11**, doi:ARTN e7745710.7554/eLife.77457 (2022).

21 Ma, J. W. *et al.* Glycogen metabolism regulates macrophage-mediated acute inflammatory responses. *Nature Communications* **11**, doi:10.1038/s41467-020-15636-8 (2020).

22 Murray, P. J. *et al.* Macrophage activation and polarization: nomenclature and experimental guidelines. *Immunity* **41**, 14-20, doi:10.1016/j.immuni.2014.06.008 (2014).

23 Brunt, E. M. *et al.* Nonalcoholic Fatty Liver Disease (NAFLD) Activity Score and the Histopathologic Diagnosis in NAFLD: Distinct Clinicopathologic Meanings. *Hepatology* **53**, 810-820, doi:10.1002/hep.24127 (2011).

24 Scott, C. L. *et al.* The Transcription Factor ZEB2 Is Required to Maintain the Tissue-Specific Identities of Macrophages. *Immunity* **49**, 312-325 e315, doi:10.1016/j.immuni.2018.07.004 (2018).

25 Zhang, C. S. *et al.* The aldolase inhibitor aldometanib mimics glucose starvation to activate lysosomal AMPK. *Nat Metab* **4**, 1369-+, doi:10.1038/s42255-022-00640-7 (2022).

26 Ben-Moshe, S. *et al.* The spatiotemporal program of zonal liver regeneration following acute injury. *Cell Stem Cell* **29**, 973-989 e910, doi:10.1016/j.stem.2022.04.008 (2022).

27 Okada, J. *et al.* Spatial hepatocyte plasticity of gluconeogenesis during the metabolic transitions between fed, fasted and starvation states. *Nat Metab* **7**, doi:10.1038/s42255-025-01269-y (2025).

28 Halpern, K. B. *et al.* Single-cell spatial reconstruction reveals global division of labour in the mammalian liver. *Nature* **542**, 352-356, doi:10.1038/nature21065 (2017).

29 Aizarani, N. *et al.* A human liver cell atlas reveals heterogeneity and epithelial progenitors. *Nature* **572**, 199-204, doi:10.1038/s41586-019-1373-2 (2019).

30 Gola, A. *et al.* Commensal-driven immune zonation of the liver promotes host defence. *Nature* **589**, 131-U285, doi:10.1038/s41586-020-2977-2 (2021).

31 Kim, A. D. *et al.* Myeloid-specific deletion of chitinase-3-like 1 protein ameliorates murine diet-induced steatohepatitis progression. *J Mol Med* **101**, 813-828, doi:10.1007/s00109-023-02325-4 (2023).

32 Higashiyama, M. *et al.* Chitinase 3-like 1 deficiency ameliorates liver fibrosis by promoting hepatic macrophage apoptosis. *Hepatology Research* **49**, 1316-1328,

doi:10.1111/hepr.13396 (2019).
33 Nishimura, N. *et al.* Chitinase 3-like 1 is a profibrogenic factor overexpressed in the aging liver and in patients with liver cirrhosis. *P Natl Acad Sci USA* **118**, doi:ARTN e201963311810.1073/pnas.2019633118 (2021).

Main figure

Figure 1. Kupffer cell death is a characteristic feature of MASLD progression

(A-D) Male Wild-type C57BL/6J mice were fed a high-fat high-cholesterol diet (HFHC) for 0, 4, or 16 weeks.

(A) KCs death was assessed by immunostaining of liver sections for Clec4f (KCs marker, green), TUNEL (red), and DAPI (nuclei, blue). Scale bar: 20μm (main panels) and 5μm (Inset).

(B) KCs death was quantified. n=4 mice/group.

(C) Flow cytometry analysis of KCs ($CD45^+$ $F4/80^{hi}$ $CD11b^{low}$ $Timd4^+$) and MoMFs ($CD45^+$ $F4/80^{low}CD11b^{hi}$ $Timd4^-$) among isolated NPCs.

(D) KCs counts were quantified. n=4-5 mice/group.

(E-F) Male wild-type C57BL/6J mice were fed either: **(E)** Normal chow diet (NCD) or high-fat diet (HFD) for 16 weeks, or **(F)** NCD or methionine-choline-deficient (MCD) diet for 6 weeks. KCs death was assessed by immunostaining of liver sections for Clec4f (green), TUNEL (red), and DAPI (nuclei, blue). Scale bar: 20μm (main panels) and 5μm (Inset). KCs death was quantified. n=4 mice/group.

Representative images are shown in A, C, E, F. One-way ANOVA (B, D). Unpaired Student's t-test (E, F). P value as indicated.

Figure 2. Kupffer cells exhibit spatially-patterned vulnerability in MASLD.

(A-E) Male Wild-type C57BL/6J mice were fed a HFHC diet for 0, 4, or 16 weeks.

(A-D) Hepatic cell death was assessed by co-staining TUNEL with: **(A)** HNF4α (hepatocytes), **(B)** Desmin (hepatic stellate cells, HSCs), **(C)** Iba1 (monocyte-derived macrophages, MoMFs), and DAPI (nuclei, blue). Scale bars: 20 μm (main panels), 5 μm (insets). Hepatic cell death was quantified (n = 4 mice/group).

(D) Zonal distribution of KCs death was evaluated by co-staining Timd4 (KCs), TUNEL, Glutamine Synthetase (GS, central vein marker) and DAPI (nuclei, blue). Scale bars: 50 μm. Zonal distribution of KCs death was quantified (n = 4 mice/group). FOV: field of view. PV: portal vein. CV: central vein.

Representative images are shown in A-D. One-way ANOVA (A-D). P value as indicated.

Figure 3 Kupffer cells exhibit metabolic reprogramming with increased glycolysis during early MASLD.

(A) Experimental design for metabolomic analysis of KCs isolated from male wild-type mice fed a HFHC diet for 0, 4 or 8 weeks. n=3 mice/group.

(B) Principal component analysis (PCA) of enriched metabolites in KCs across different dietary durations.

(C-D) Kyoto Encyclopedia of Genes and Genomes (KEGG) pathway enrichment analysis of metabolic pathways upregulated in KCs at 4 weeks **(C)** or 8 weeks **(D)**. The glucose metabolism

pathway is highlighted by red rectangles.

(E) Heatmap depicting significantly altered metabolites involved in glucose metabolism pathways in KCs across different dietary durations.

(F) Heatmap depicting significantly altered metabolites involved in cell death in KCs across different dietary durations.

Figure 4. Excessive glucose metabolic activity contributes to Kupffer cell death.

(A-B) Isolated KCs were treated for 24 h with: 5.5 mM glucose + isopropanol (control), 5.5 mM glucose + 800 μM palmitic acid (PA), 10 mM glucose + 800 μM PA. Cell viability was assessed by Cleaved caspase-3 (Cl-Casp3) staining (Cl-Casp3^{+} cells = dead). Scale bars: 20 μm (main panels), 5 μm (insets). Cl-Casp3 was detected by Western blot.

(C-D) Isolated Kupffer cells were treated for 24 h with: Blank (no treatment), DMSO (vehicle control), 20 μM PS48 (PDK1 activator). Scale bars: 20 μm (main panels), 5 μm (insets). Cell death were analyzed as above.

(E-F) Isolated Kupffer cells were treated for 24 h with: Blank (no treatment), DMSO (vehicle control), 20 μM oligomycin (Oligo, ATP synthase inhibitor). Scale bars: 20 μm (main panels), 5 μm (insets). Cell death were analyzed as above.

One-way ANOVA (A, C, E). P value as indicated.

Figure 5. Enhanced glycolytic flux in Chi3l1$^{-/-}$ macrophages.

(A) Schematic diagram depicting the fate of glucose-derived ribose carbons in WT mouse primary hepatocytes.

(B) Principal component analysis (PCA) of metabolites in WT and Chil1$^{-/-}$ BMDMs cultured with [U-^{13}C]glucose.

(C) Heatmap depicting significantly altered Glycolysis and Pentose phosphate (PPP) metabolites in WT and Chil1$^{-/-}$ BMDMs.

(D) Glucose metabolic flux analysis in WT and Chil1$^{-/-}$ BMDMs cultured with [U-^{13}C]glucose showing mass isotopologue distributions of: Glycolytic intermediates (Glc, F6P, FBP, 3PGA, 2PGA, PEP, PA, LA, G6P). PPP intermediates (Ru5P, R5P, S7P, DHAP). Data represent n= 6 biological replicates/group.

(E-F) Extracellular acidification rate (ECAR) analysis of WT or Chil1$^{-/-}$ BMDMs cells. BMDM were sequentially treated with Glucose, oligomycin and 2-DG as indicated during seahorse.

Figure 6. Enhanced glycolysis accelerated Kupffer cell death during MASLD.

(A) Cleaved caspase-3 (Cl-Casp3) staining to detect WT and Chil1$^{-/-}$ Kupffer cell death. Cells were under treatment without (Blank) or with either Isopropyl alcohol (Iso) or Palmitic Acid (PA) for 24 h. Scale bar: 20μm.

(B) Cl-Casp3+ cells were quantified.

(C) LDH release measurement in culture medium of KCs isolated from male WT and Chil1$^{-/-}$ mice was measured after treatment for 24 h with: Blank (no treatment), ISO (vehicle control), 800 μM PA.

(D) Flow cytometry analysis of KCs (CD45^{+} F4/80^{hi} CD11b^{low} Timd4^{+}) and MoMFs (CD45^{+} F4/80^{low} CD11b^{hi} Timd4^{-}) among NPCs in Clec4f-cre and Clec4f$^{\Delta Chil1}$ mice fed HFHC diet for 0 or 16 weeks.

619 **(E)** KCs counts were quantified. n= 4 mice/group.
620 **(F)** Kupffer cell death was assessed by immunostaining of Timd4 (KCs marker, green), TUNEL
621 (red), and DAPI (nuclei, blue) in liver sections from Clec4f-cre and Clec4f$^{\Delta Chil1}$ mice fed HFHC diet
622 for 0 or 16 weeks. Scale bar: 20μm (main panels) and 5μm (Inset).
623 **(G)** KCs death was quantified. n=4 mice/group.
624 Representative images shown (A, D, F). Unpaired student t-test (B,C,E,G). P value as indicated.
625
626 **Figure 7. Excessive glycolysis enhancement promotes Kupffer cell death in MASLD.**
627 **(Left)** Under physiological conditions, Kupffer cells (KCs) maintain basal glucose metabolism
628 supporting cellular homeostasis and survival.
629 **(Right)** During MASLD progression, KCs undergo excessive glycolysis enhancement, which
630 accelerates KCs death.

Figure 1

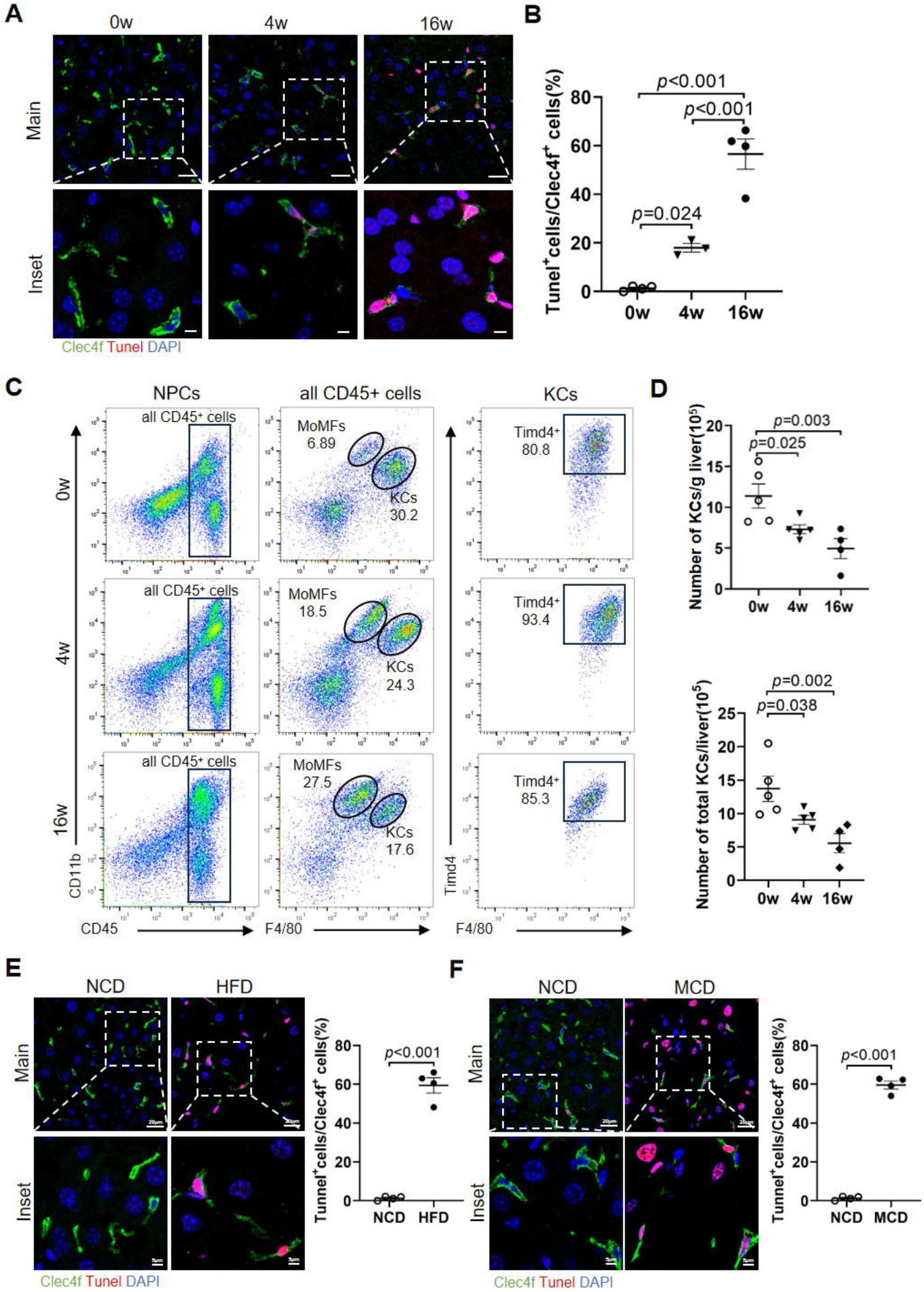
A
0w
4w
16w
Main
Inset
Clec4f Tunel DAPI
B
Tunel+cells/Clec4f+ cells(%)
p<0.001
p<0.001
p=0.024
0w
4w
16w
C
NPCs
all CD45+ cells
KCs
all CD45+ cells
MoMFs 6.89
KCs 30.2
Timd4+ 80.8
MoMFs 18.5
KCs 24.3
Timd4+ 93.4
MoMFs 27.5
KCs 17.6
Timd4+ 85.3
CD11b
CD45
F4/80
Timd4
D
Number of KCs/g liver(10^5)
p=0.003
p=0.025
Number of total KCs/liver(10^5)
p=0.002
p=0.038
E
NCD
HFD
Tunel+cells/Clec4f+ cells(%)
p<0.001
F
NCD
MCD
p<0.001

Figure 2

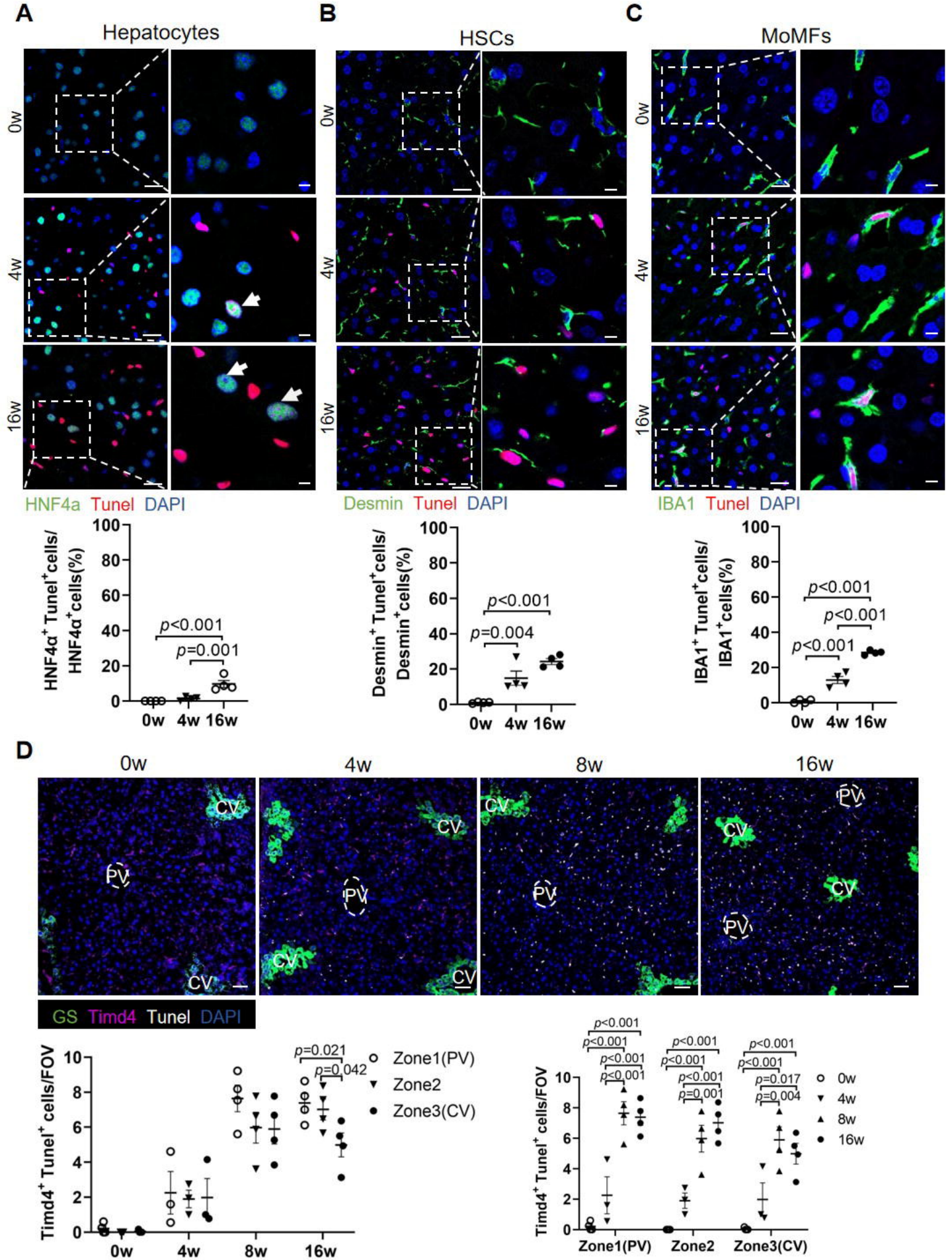
A
Hepatocytes
B
HSCs
C
MoMFs
0w
4w
16w
HNF4a Tunel DAPI
Desmin Tunel DAPI
IBA1 Tunel DAPI
HNF4α+ Tunel+cells/ HNF4α+cells(%)
Desmin+ Tunel+cells/ Desmin+cells(%)
IBA1+ Tunel+cells/ IBA1+cells(%)
p<0.001
p=0.001
p=0.004
0w 4w 16w
D
0w
4w
8w
16w
CV
PV
GS Timd4 Tunel DAPI
Timd4+ Tunel+ cells/FOV
Zone1(PV)
Zone2
Zone3(CV)
p=0.021
p=0.042
p=0.017
p=0.004

Figure 3

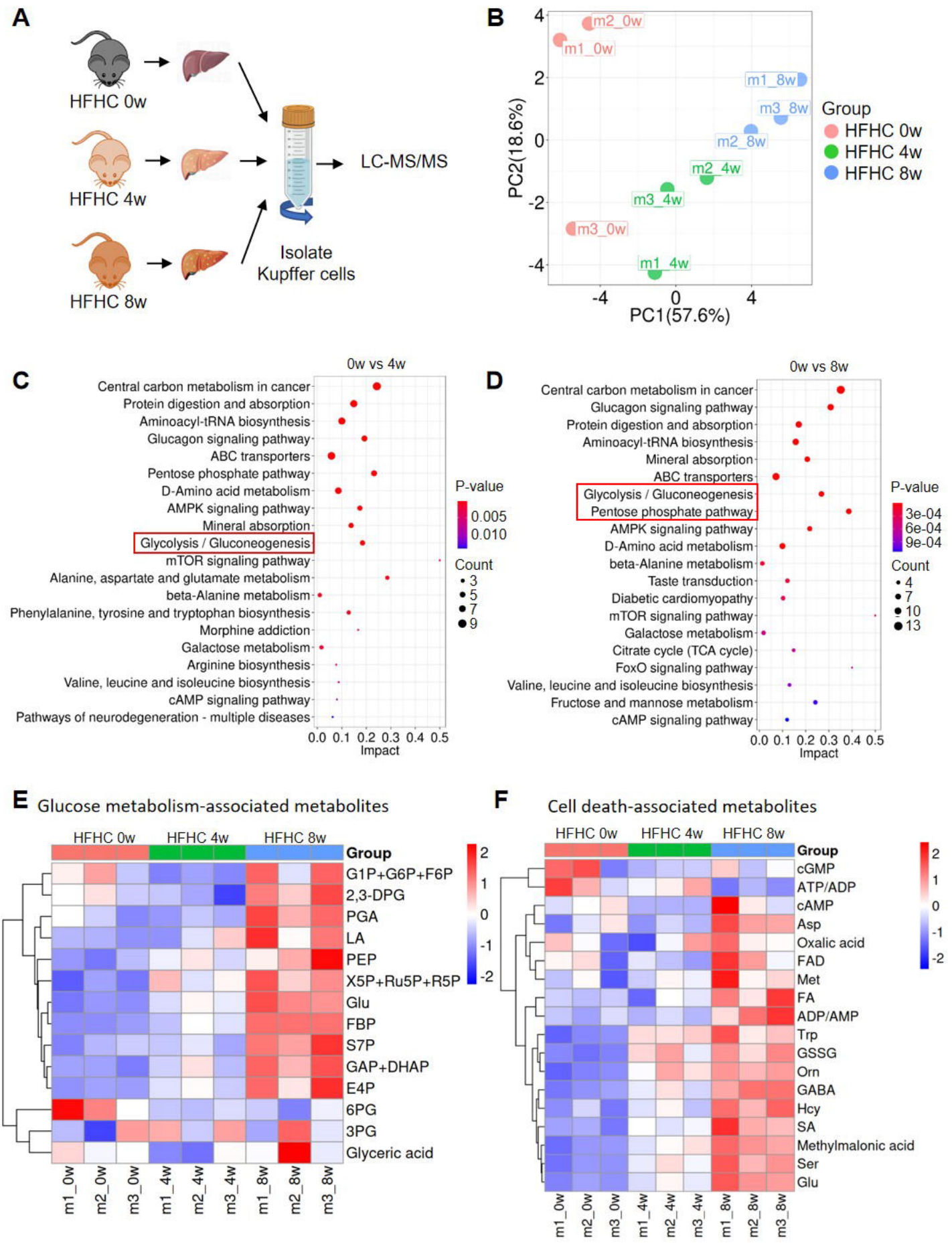
A
HFHC 0w
HFHC 4w
HFHC 8w
LC-MS/MS
Isolate
Kupffer cells
B
m2_0w
m1_0w
m1_8w
m3_8w
m2_8w
m2_4w
m3_4w
m3_0w
m1_4w
PC2(18.6%)
PC1(57.6%)
Group
HFHC 0w
HFHC 4w
HFHC 8w
C
0w vs 4w
Central carbon metabolism in cancer
Protein digestion and absorption
Aminoacyl-tRNA biosynthesis
Glucagon signaling pathway
ABC transporters
Pentose phosphate pathway
D-Amino acid metabolism
AMPK signaling pathway
Mineral absorption
Glycolysis / Gluconeogenesis
mTOR signaling pathway
Alanine, aspartate and glutamate metabolism
beta-Alanine metabolism
Phenylalanine, tyrosine and tryptophan biosynthesis
Morphine addiction
Galactose metabolism
Arginine biosynthesis
Valine, leucine and isoleucine biosynthesis
cAMP signaling pathway
Pathways of neurodegeneration - multiple diseases
Impact
P-value
0.005
0.010
Count
3
5
7
9
D
0w vs 8w
Central carbon metabolism in cancer
Glucagon signaling pathway
Protein digestion and absorption
Aminoacyl-tRNA biosynthesis
Mineral absorption
ABC transporters
Glycolysis / Gluconeogenesis
Pentose phosphate pathway
AMPK signaling pathway
D-Amino acid metabolism
beta-Alanine metabolism
Taste transduction
Diabetic cardiomyopathy
mTOR signaling pathway
Galactose metabolism
Citrate cycle (TCA cycle)
FoxO signaling pathway
Valine, leucine and isoleucine biosynthesis
Fructose and mannose metabolism
cAMP signaling pathway
Impact
P-value
3e-04
6e-04
9e-04
Count
4
7
10
13
E Glucose metabolism-associated metabolites
HFHC 0w
HFHC 4w
HFHC 8w
Group
G1P+G6P+F6P
2,3-DPG
PGA
LA
PEP
X5P+Ru5P+R5P
Glu
FBP
S7P
GAP+DHAP
E4P
6PG
3PG
Glyceric acid
m1_0w
m2_0w
m3_0w
m1_4w
m2_4w
m3_4w
m1_8w
m2_8w
m3_8w
F Cell death-associated metabolites
HFHC 0w
HFHC 4w
HFHC 8w
Group
cGMP
ATP/ADP
cAMP
Asp
Oxalic acid
FAD
Met
FA
ADP/AMP
Trp
GSSG
Orn
GABA
Hcy
SA
Methylmalonic acid
Ser
Glu
m1_0w
m2_0w
m3_0w
m1_4w
m2_4w
m3_4w
m1_8w
m2_8w
m3_8w

Figure 4

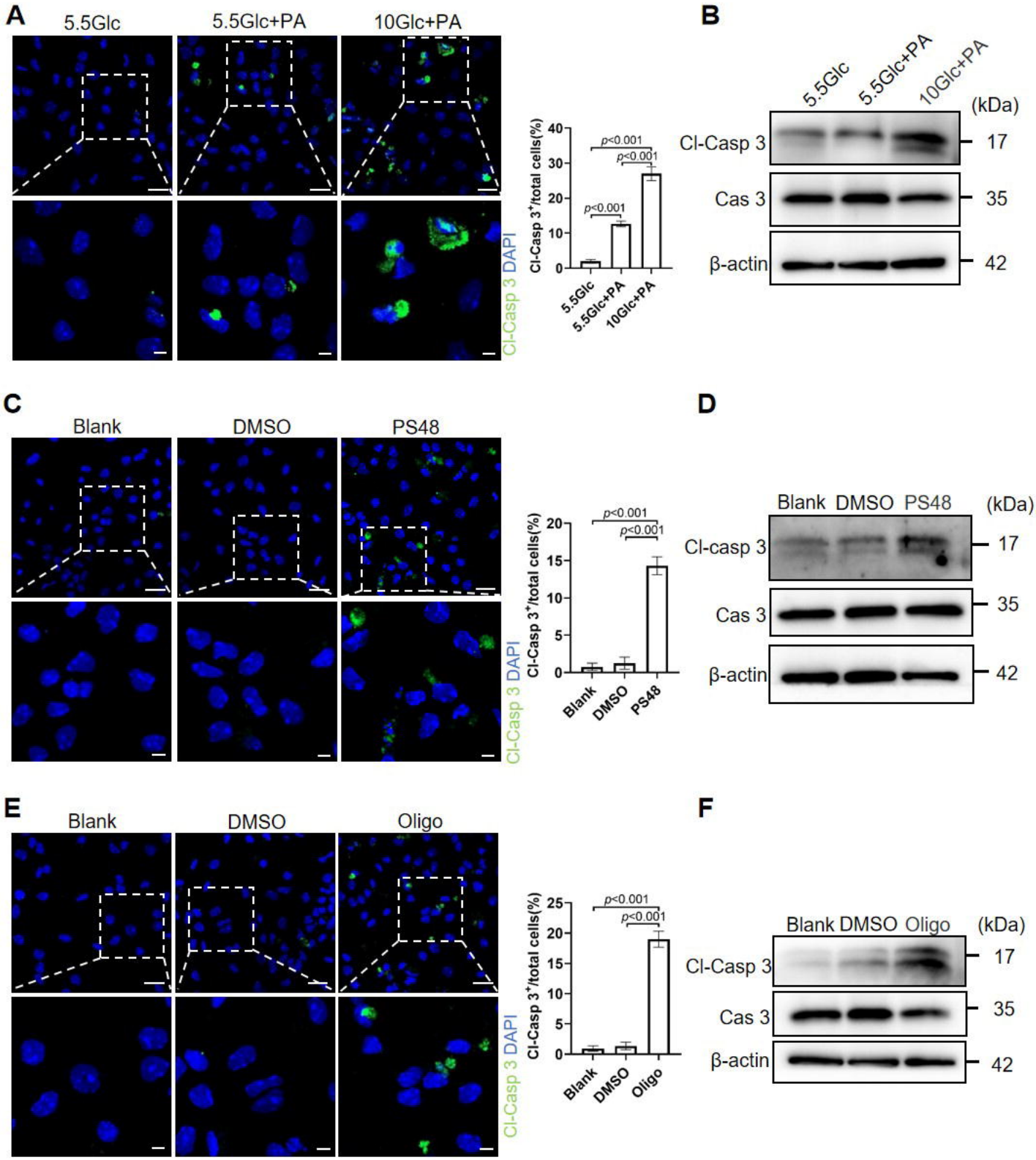
A
5.5Glc
5.5Glc+PA
10Glc+PA
Cl-Casp 3 DAPI
Cl-Casp 3+/total cells(%)
p<0.001
p<0.001
p<0.001
5.5Glc
5.5Glc+PA
10Glc+PA
B
5.5Glc
5.5Glc+PA
10Glc+PA
(kDa)
Cl-Casp 3
Cas 3
β-actin
17
35
42
C
Blank
DMSO
PS48
Cl-Casp 3 DAPI
Cl-Casp 3+/total cells(%)
p<0.001
p<0.001
Blank
DMSO
PS48
D
Blank DMSO PS48
(kDa)
Cl-casp 3
Cas 3
β-actin
17
35
42
E
Blank
DMSO
Oligo
Cl-Casp 3 DAPI
Cl-Casp 3+/total cells(%)
p<0.001
p<0.001
Blank
DMSO
Oligo
F
Blank DMSO Oligo
(kDa)
Cl-Casp 3
Cas 3
β-actin
17
35
42

Figure 5

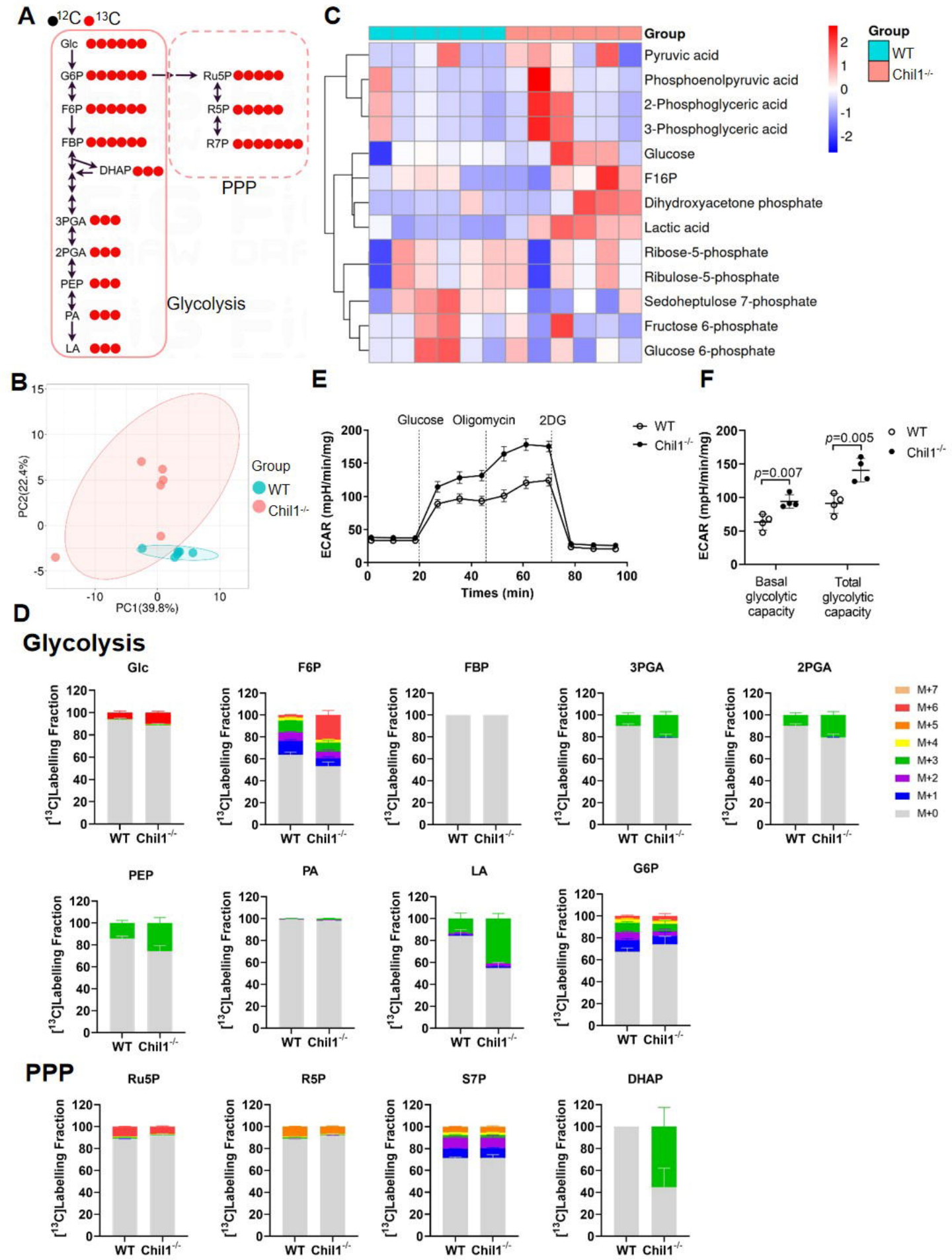
A
12C 13C
Glc
G6P
F6P
FBP
DHAP
3PGA
2PGA
PEP
PA
LA
Glycolysis
Ru5P
R5P
R7P
PPP
C
Group
Pyruvic acid
Phosphoenolpyruvic acid
2-Phosphoglyceric acid
3-Phosphoglyceric acid
Glucose
F16P
Dihydroxyacetone phosphate
Lactic acid
Ribose-5-phosphate
Ribulose-5-phosphate
Sedoheptulose 7-phosphate
Fructose 6-phosphate
Glucose 6-phosphate
WT
Chil1-/-
B
PC2(22.4%)
PC1(39.8%)
Group
WT
Chil1-/-
E
Glucose
Oligomycin
2DG
ECAR (mpH/min/mg)
Times (min)
WT
Chil1-/-
F
ECAR (mpH/min/mg)
p=0.007
p=0.005
Basal glycolytic capacity
Total glycolytic capacity
WT
Chil1-/-
D
Glycolysis
Glc
F6P
FBP
3PGA
2PGA
PEP
PA
LA
G6P
[13C]Labelling Fraction
WT
Chil1-/-
M+7
M+6
M+5
M+4
M+3
M+2
M+1
M+0
PPP
Ru5P
R5P
S7P
DHAP

Figure 6

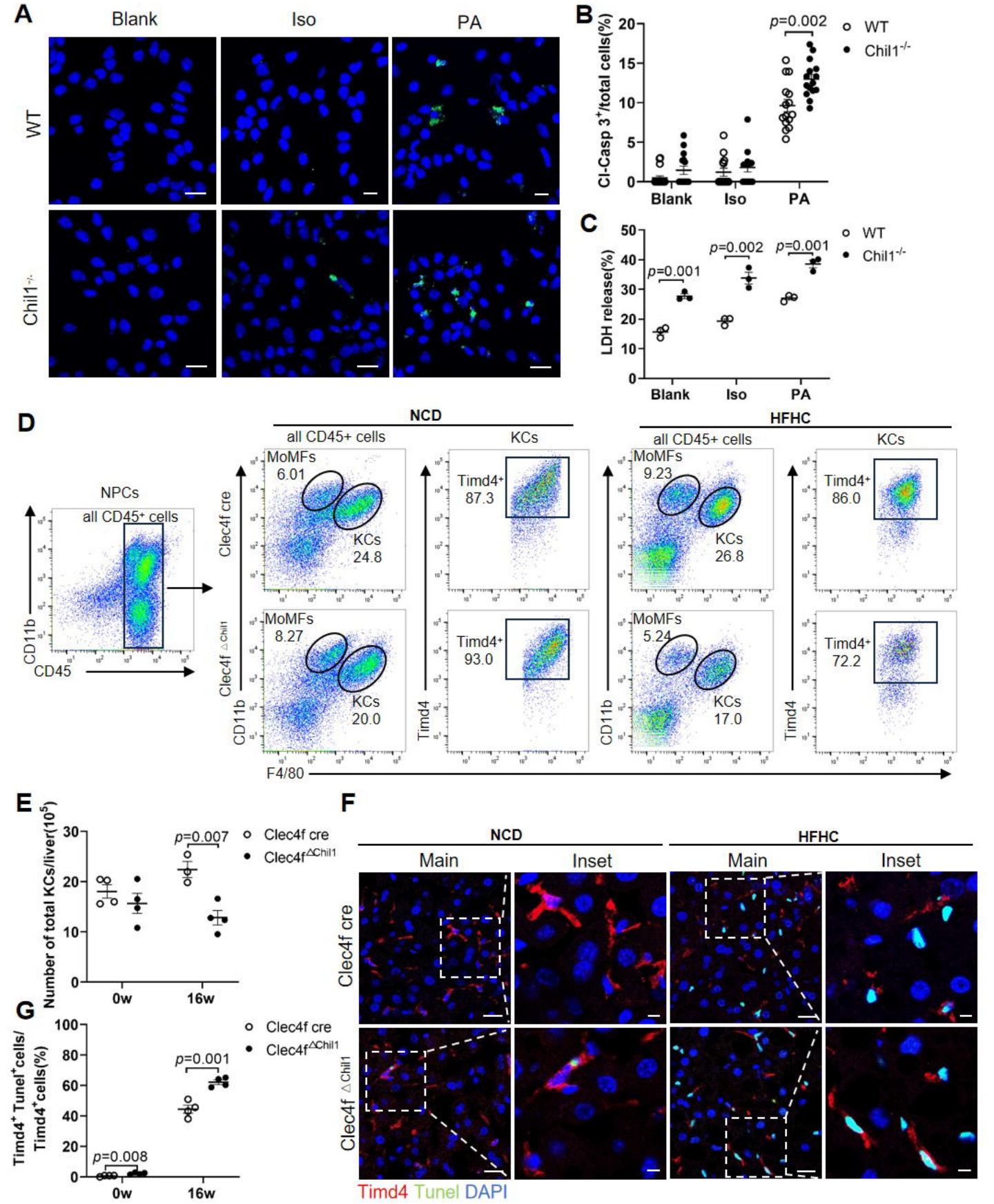
A
Blank
Iso
PA
WT
Chil1-/-
B
Cl-Casp 3+/total cells(%)
p=0.002
WT
Chil1-/-
Blank
Iso
PA
C
LDH release(%)
p=0.001
p=0.002
p=0.001
WT
Chil1-/-
Blank
Iso
PA
D
NCD
HFHC
all CD45+ cells
KCs
NPCs
all CD45+ cells
CD11b
CD45
Clec4f cre
Clec4f ΔChil1
MoMFs
6.01
KCs
24.8
MoMFs
8.27
KCs
20.0
Timd4+
87.3
Timd4+
93.0
MoMFs
9.23
KCs
26.8
MoMFs
5.24
KCs
17.0
Timd4+
86.0
Timd4+
72.2
Timd4
F4/80
E
Number of total KCs/liver(10^5)
p=0.007
Clec4f cre
Clec4f ΔChil1
0w
16w
G
Timd4+ Tunel+cells/ Timd4+cells(%)
p=0.001
p=0.008
Clec4f cre
Clec4f ΔChil1
0w
16w
F
NCD
HFHC
Main
Inset
Main
Inset
Clec4f cre
Clec4f ΔChil1
Timd4 Tunel DAPI

Figure 7

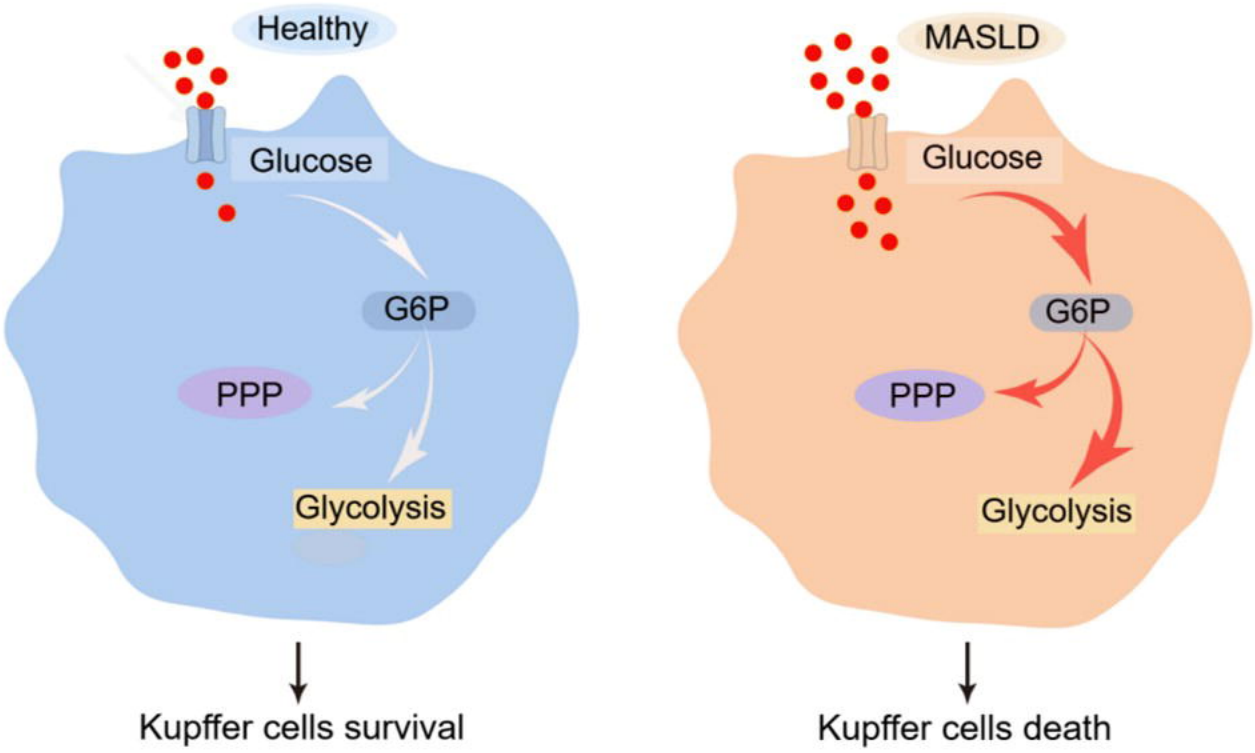
Healthy
Glucose
G6P
PPP
Glycolysis
Kupffer cells survival
MASLD
Glucose
G6P
PPP
Glycolysis
Kupffer cells death